Letter

Observing octupolar charge orders and their transition dynamics in Coulomb clusters

Akhil Ayyadevara [1,*] Anand Prakash [1] Shovan Dutta [1] Arun Paramekanti [2] and S. A. Rangwala [1]

[1] *Raman Research Institute, C. V. Raman Avenue, Sadashivanagar, Bangalore 560080, India*

[2] *Department of Physics, University of Toronto, 60 St. George Street, Toronto, Ontario, Canada M5S 1A7*

(Received 17 October 2025; accepted 9 February 2026; published 18 March 2026)

Interacting many-particle systems can self-organize into a rich variety of crystalline structures. While symmetry provides a powerful framework for predicting whether transitions between crystal states are continuous or discontinuous, collective lattice dynamics offer complementary insights into the microscopic mechanisms that drive these transitions. Trapped laser-cooled ions present a pristine and highly controllable system for studying this interplay of symmetry and dynamics. Here, we use real-time fluorescence imaging while deforming the trap potential to observe a variety of structural transitions in three-dimensional (3D), unit-cell-like ion clusters. We identify a set of unexplored transitions signaled by parity-odd octupole order parameters and probe their distinct dynamical signatures. Our experiments reveal the softening of a collective Higgs-like mode, indicating spontaneous symmetry breaking, hysteresis resulting from a catastrophe where a metastable state vanishes abruptly, and stochastic switching between metastable states of distinct symmetries. We also uncover a remarkable coincidence of symmetry-breaking and discontinuous transitions, analogous to a thermodynamic triple point. Our results establish 3D trapped-ion clusters as a versatile platform for engineering complex potential energy landscapes, opening avenues for studying collective phenomena such as geometric frustration with multipolar orders and the stochastic kinetics of rare events in exotic mesoscopic settings.

DOI: 10.1103/2rs1-c5r1

Introduction. Phase transitions are ubiquitous in nature, occurring at energy scales ranging from those relevant to solids [1] and biological systems [2] to the extreme conditions found in particle colliders and the early universe [3]. Our understanding of equilibrium phase transitions rests on the foundational framework of Landau theory [4], where symmetry plays a key role in sculpting the free-energy landscape, which dictates the nature of the transition. On the other hand, the real-time transformation from one state to another is governed by dynamical pathways, which can be strikingly different for continuous and first-order transitions. Recent experiments in ultrafast diffraction and engineered light-matter interactions have begun to provide insights into transition pathways in dynamics of chemical reactions [5], atomically resolved crystal dynamics in solid-state materials [6–8], and self-organization in atom-cavity systems [9]. Understanding such transition mechanisms in relation to the underlying symmetry transformations is important for steering molecular reactions [5] and for the dynamical control of quantum materials [7,8].

The rich interplay of symmetry and dynamics is exemplified by two different kinds of crystal transitions in a solid. Small atomic displacements can trigger a continuous transition to a lower-symmetry configuration, called *displacive* transitions [10]. These are dynamically signaled by the softening of an optical phonon mode, as observed for the α–β transition in quartz [11] and in ferroelectrics such as $BaTiO_3$ [12,13]. In contrast, crystals can also undergo a discontinuous transition to a state with a different point-group symmetry, accompanied by complex atomic rearrangements [14]. The dynamics near such *reconstructive* transitions are characterized by metastability and hysteresis [15,16] due to barriers [17] in the free-energy landscape. A single system that can realize a variety of crystalline states with diverse symmetries can provide a unified platform to study and compare the dynamics of distinct crystal transitions.

Trapped-ion Coulomb crystals offer such a versatile and tunable platform [18–22] for experimental investigations of structural phase transitions from few-body clusters [23–26] to mesoscopic ensembles [27–30]. The ions can self-organize into a multitude of charge orders depending on the competition between the external confinement and Coulomb repulsion. Fluorescence from Doppler-cooling lasers enables spatially resolved imaging of individual ions and tracking of the real-time crystal configuration. The ability to excite and probe collective vibrational modes [31,32] enables the investigation of crystal dynamics near structural transitions, which was used to study the linear to zigzag transition in ion chains [32–34]. In addition, the buckling of two-dimensional (2D) Coulomb crystals has been proposed to realize unconventional clock-model transitions [35].

Here, we experimentally realize and probe the dynamics of a distinct class of structural transitions in three-dimensional (3D) unit-cell-like trapped-ion clusters. By tuning the anisotropy of the confinement, we steer the clusters through various regions of stability, uncovering configurations of dif-

*Contact author: akhilv@rri.res.in

Published by the American Physical Society under the terms of the Creative Commons Attribution 4.0 International license. Further distribution of this work must maintain attribution to the author(s) and the published article's title, journal citation, and DOI.

ferent symmetries across both *displacive* and *reconstructive* transitions. In particular, we identify a set of transitions characterized by parity-odd octupole moments. Such symmetry breaking involving higher-order multipoles is of significant interest in the context of "hidden orders" in correlated quantum materials [36–39] and for shape transitions of heavy nuclear isotopes [40–42]. We directly observe the softening of a collective vibrational mode, signaling a transition of the energy landscape from a Mexican hat potential to a potential with a single minimum. This mechanism is analogous to the softening of a Higgs-like mode across a continuous phase transition. We also observe hysteresis arising from a dynamical catastrophe, where a stable equilibrium suddenly vanishes from the landscape. Furthermore, we find a triple-point-like feature and noise-induced configuration switching between metastable states, highlighting the complex energy landscapes realizable in finite-sized 3D ion clusters.

Structural transitions. We trap clusters of laser-cooled $^{40}Ca^{+}$ ions [43] in an end-cap-type radio-frequency (rf) trap [44,45]. The trap provides a time-averaged harmonic confinement in 3D with cylindrical symmetry (see Supplemental Material [46]). The competition between Coulomb interactions and the harmonic confinement determines the equilibrium configuration(s) of minimum energy [CME(s)] [47], which minimize

$$V = \sum_{i=1}^{n} \left[\frac{m\omega_x^2}{2} \left(x_i^2 + y_i^2 + \alpha^2 z_i^2 \right) + \sum_{j>i}^{n} \frac{k_e e^2}{|\boldsymbol{r}_i - \boldsymbol{r}_j|} \right], \quad (1)$$

where $\boldsymbol{r}_i \equiv (x_i, y_i, z_i)$, $i = 1, 2, \ldots, n$, are the coordinates of the ions with mass m, $k_e = 1/4\pi\epsilon_0$ is the Coulomb constant, e is the elementary charge, ω_x and ω_z are the secular frequencies along azimuthal and axial directions, respectively, and $\alpha = \omega_z/\omega_x$ is the aspect ratio of the 3D potential. In the experiment, we tune this anisotropy α by changing a superimposed dc voltage U_{dc} (see Supplemental Material [46]). We track the resulting sequence of configurations and their transitions for four-, five-, and six-ion clusters via fluorescence imaging, capturing 2D projections of the cluster configurations as shown in Fig. 1. Due to the cylindrical trap symmetry and photon kicks from the Doppler cooling laser, these ion clusters freely rotate around the z axis over the imaging integration time. At $\alpha = 1$, the trap potential is isotropic, and the ion clusters undergo free spherical rotation. As seen from Fig. 1, for $\alpha \gg 1$, the ions assume 2D configurations in the x-y plane, while decreasing α leads to transitions into various 3D structures, eventually yielding a one-dimensional chain along z axis for $\alpha \ll 1$.

To characterize the observed transitions, we have calculated the CMEs for four-, five-, and six-ion clusters and their normal modes in the zero-temperature limit (see Appendix D and Figs. S4, S5, and S6 in the Supplemental Material [46]). Our numerical calculations yield CMEs that match the experimentally observed structures and enable us to accurately determine the value of α corresponding to the structural transition points. Focusing on the regime of $\alpha > 1$, we unearth rich dynamics that emerge near three distinct types of octupolar transitions highlighted in Fig. 1(a). They are distinguished by characteristic signatures in the low-lying collective modes, shown in Fig. 1(b): (i) a symmetry-breaking transition in a four-ion cluster with mode softening on both sides of the

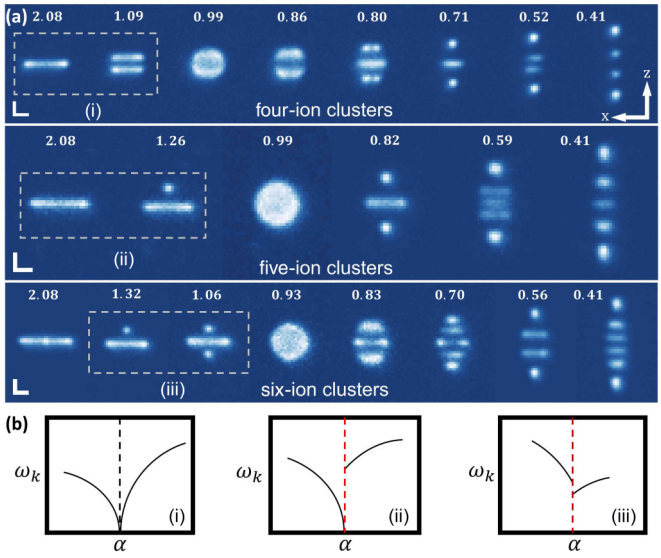


FIG. 1. Structural transitions in a 3D trap. (a) Stitched images of all the observed four-, five-, and six-ion clusters labeled by corresponding $\alpha = \omega_z/\omega_x$ (see Supplemental Material [46]). The scale bar represents 5 μm. (b) Sketches of characteristic low-lying normal modes for the three transitions of interest identified in the dashed boxes in panel (a).

critical point, (ii) a coincidence of buckling instability of a 2D configuration and a reconstructive transition to a 3D configuration in a five-ion cluster, and (iii) a discontinuous transition in a six-ion cluster, where 3D configurations of two different symmetries are bistable over an extended region.

Higgs-like mode softening. For $\alpha \gg 1$, four ions self-organize at the corners of a square in the x-y plane. As the axial confinement is made weaker by lowering α, the square transitions to a tetrahedral arrangement. The two diagonals of the square, represented by the solid and the dashed *pseudo*bonds in Fig. 2(a), *displace* along the axial direction. This breaks inversion symmetry about the trap center at the critical point $\alpha_c \approx 1.216$ (derivation in the Supplemental Material [46]), realizing a supercritical pitchfork bifurcation [48]. The lowest-order multipole that captures this inversion-breaking transition is the (complex) parity-odd octupole moment $\psi_{32} \equiv \int d\mathbf{r} \rho_e(\mathbf{r}) Y_{3,2}(\mathbf{r})$, where $Y_{3,2}(\mathbf{r}) \propto (x + iy)^2 z$ and $\rho_e(\mathbf{r})$ is the charge distribution.

The numerically computed spectrum of the low-frequency collective modes in the vicinity of α_c is plotted in Fig. 2(c). On both sides of the transition, we observe a zero-frequency mode corresponding to the free rotation about the z axis and a mode that softens at α_c. On the tetrahedral side, this zero mode and soft mode correspond to phase and amplitude fluctuations of the octupolar order parameter ψ_{32}, i.e., direct analogues of Goldstone and Higgs modes in the language of phase transitions.

Experimentally, we can couple to $|\psi_{32}|^2$ by modulating the trap rf voltage. This modulation effectively drives the soft mode of the tetrahedron (see Appendix A) and leads to a blurring in the spacing between the upper and lower arms [see Fig. 2(b)]. Such coupling to the absolute value of the order parameter is an established route to exciting Higgs-like

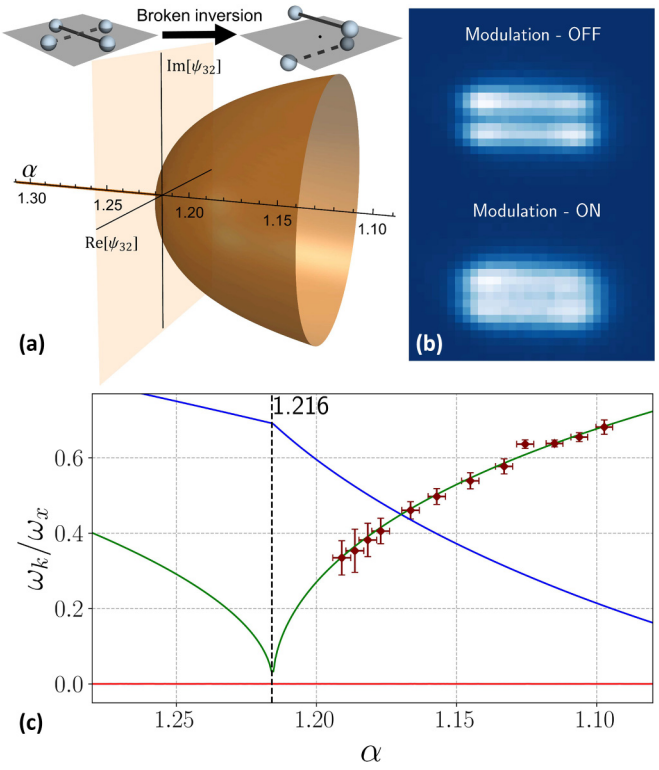


FIG. 2. Resonant excitation of a Higgs-like soft mode of a four-ion tetrahedron. (a) The square-to-tetrahedron transition visualized as a supercritical pitchfork bifurcation in the octupole moment ψ_{32}. (b) Excitation of the soft mode of the tetrahedral cluster via trap-voltage modulation captured by the fluorescence images. (c) Spectra of low-frequency normal modes (ω_k) computed around the critical point. Red line corresponds to the zero-frequency free rotation about the z axis. Blue curve corresponds to two degenerate rotational modes about the x and y axes (see Table I in Appendix A). The green curve corresponds to the inversion symmetry-breaking (restoring) mode of the square (tetrahedron), softening at $\alpha \approx 1.216$. The experimentally measured Higgs-like soft mode on the tetrahedron side (red dots) falls on top of the computed spectrum. Vertical error bars are 1σ spread around the peak response frequency of the cluster (see Fig. 6 in Appendix A). Horizontal error bars show uncertainty in the value of α measured by exciting the motion of a single ion.

modes [49,50]. Over a significant range of α, we find that the peak response frequency is in excellent agreement with the numerically computed soft-mode spectrum, as seen from Fig. 2(c).

We note that it is difficult to explore the regime very close to the transition point since it becomes increasingly harder to distinguish the perturbed and unperturbed images as the separation between the arms of the tetrahedron becomes smaller than the possible image resolution. We also cannot excite the out-of-plane soft mode of the square for $\alpha > \alpha_c$ with the trap-voltage modulation, as the drive in this case couples predominantly to a high-frequency in-plane breathing mode (see Appendix A).

Hysteresis and a triple point. The planar CME of the five-ion cluster for $\alpha \gg 1$ is a regular pentagon in the x-y plane. As α is reduced, the pentagon transitions to a square-base pyramid with the apex ion on the z axis (see Fig. 3). The lowest-order multipole that distinguishes these configurations is the real, parity-odd octupole moment $\psi_{30} \equiv \int d\mathbf{r}\rho_e(\mathbf{r})Y_{3,0}(\mathbf{r})$, where $Y_{3,0}(\mathbf{r}) \propto 5z^3 - 3r^2z$. This vanishes for the pentagon and takes on positive (negative) values for the pyramid with the apical ion at $z > 0$ ($z < 0$). Below, we discuss the complex energy landscape for this five-ion cluster, obtained numerically via the nudged elastic band (NEB) technique [51] (see Appendix D), and correlate this with our experimental measurement of the hysteretic dynamics of $|\psi_{30}|$.

The global minimum shifts between the pentagon and the pyramid at $\alpha_t \approx 1.328$, marked by a discontinuous jump in the normal-mode spectrum (see Supplemental Material [46]). Surprisingly, two out-of-plane vibrational modes of the pentagon also soften close to this transition point via a supercritical pitchfork bifurcation, as shown in Fig. 3(a). The analytically obtained critical point (α_c) of this buckling instability (see Appendix B) matches the *reconstructive* transition point, $\alpha_c \simeq \alpha_t$. This feature is analogous to a triple point in thermodynamic phase transitions [52], where a *displacive* and a *reconstructive* transition occur simultaneously. In addition, the two degenerate, buckled pentagons survive as local minima over a small window before vanishing via saddle-node bifurcation at $\alpha^* \approx 1.29$ [Fig. 3(a)]. In contrast, the pyramid remains stable until $\alpha \approx 1.59$, where it continuously transitions to a planar metastable state: a square in the x-y plane with one ion at the trap center [21]. This asymmetry in the stability of two metastable CMEs (pentagon versus square pyramid) gives rise to a prominent hysteresis.

By applying triangular voltage ramps, we drive the five-ion cluster back and forth in a series of axial compression and decompression cycles. In each ramp, as the axial confinement is weakened, the pentagon sharply transitions to a square pyramid beyond α_t with the apical ion in the pyramid randomly appearing at $z > 0$ or $z < 0$. This is signaled by the sudden increase in $|\psi_{30}|$ with decreasing α (rightward sweep) as shown in Fig. 3(b). However, when the cluster is axially compressed by increasing α (leftward sweep), the pyramidal structure remains intact well beyond α_t, as the system remains trapped in a local minimum. This phenomenon is analogous to the well-known example of metastable supercooled water. A photon kick or background collision triggers a nucleation-like event into the pentagonal ground state. These events occur over a broad range of α, where the order parameter ψ_{30} randomly jumps to zero. The resulting hysteresis loop is strongly asymmetric as seen from Fig. 3(b). Real-time experimental videos demonstrating fast and slow nucleation events are provided in the Supplemental Material [46].

Stochastic configuration switching. In the six-ion cluster, a *reconstructive* transition is observed between two 3D structures with distinct symmetries: A pentagonal pyramid with one apex ion on the z axis switches to an octahedron (square bipyramid) with the two apex ions on the z axis, as shown in Fig. 4. The lowest-order multipole that distinguishes these configurations is again the real, parity-odd octupole moment ψ_{30}, which vanishes for the octahedron and takes on positive (negative) values for the pyramid with the apical ion at $z > 0$ ($z < 0$).

The energy landscape obtained via the NEB method is shown in Fig. 4(a). The octahedron emerges as a stable node

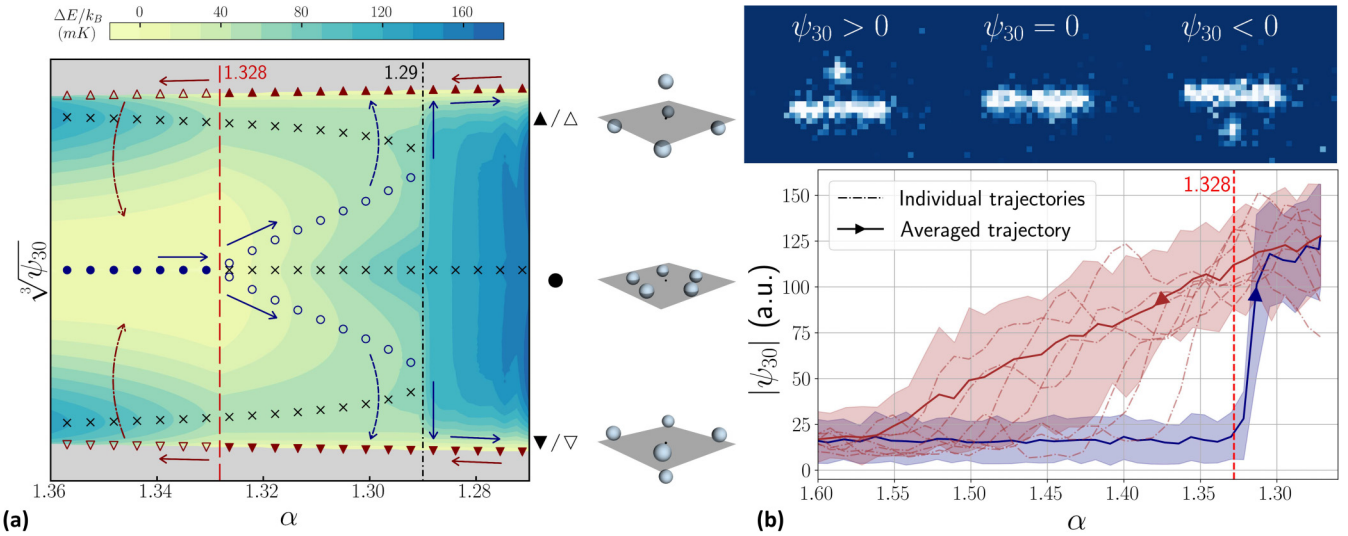


FIG. 3. Hysteresis and a triple point in five-ion structural transition landscape. (a) The numerically computed potential energy surface around the planar-to-3D transition in a five-ion cluster as a function of α and the octupole order parameter ψ_{30}. For a clearer visual representation, we use $\sqrt[3]{\psi_{30}}$ rather than ψ_{30} for the y axis. The solid symbols represent global minima, the open symbols represent metastable minima, and the crosses represent saddles. The solid arrows mark the *flow* of the cluster state along the global minimum as the cluster is cycled across the transition points. The dashed arrows represent possible locations where noise-induced barrier hopping events occur. (b) (Top) Fluorescence images from the experiment while cycling the cluster across the transition via linear voltage ramps. The duration of each forward/backward ramp is 5 s. (Bottom) Octupole moment ψ_{30} computed from 3D reconstructed images using Abel transforms (see Appendix C). The solid lines show averaged trajectories over 90 such scans, with arrows marking the direction of the ramp. The dot-dashed lines show a few backward sweeps where the pyramidal cluster changes abruptly to the pentagonal ground state over a wide range of α. The shaded region represents the 16th and the 84th percentiles around the averaged trajectory.

via a subcritical pitchfork bifurcation at $\alpha \approx 1.46$. The global minimum shifts between the pentagonal pyramid and the octahedron at $\alpha \approx 1.238$, and is also marked by a discontinuous jump in the normal-mode spectra (see Supplemental Material [46]). The two pyramids vanish from the potential landscape at $\alpha \approx 1.19$ via saddle-node bifurcations. The extended region of tristability between the octahedron and the two pentagon-pyramids leads to stochastic switching of the cluster configuration.

We experimentally track the dynamics of ψ_{30} close to the *reconstructive* transition point, where all the minima have equal energy. Figure 4(b) shows the time trace of ψ_{30} obtained at $\alpha \approx 1.24$, which exhibits the expected three-state telegraph-like switching dynamics. We provide the video corresponding to the time trace in the Supplemental Material [46].

Conclusions and outlook. We have investigated three distinct dynamical signatures of structural transitions in unit-cell-like 3D trapped-ion clusters. While our system lacks the

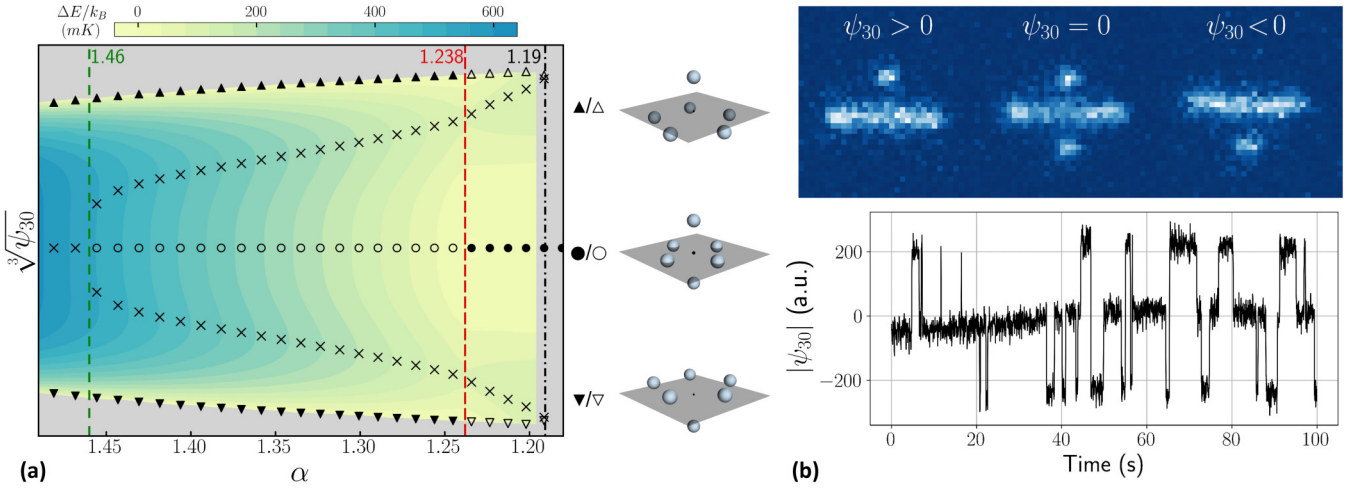


FIG. 4. Stochastic switching between metastable configurations of a six-ion cluster. (a) Energy landscape around the *reconstructive* transition between pentagonal pyramids and a square bipyramid, shown as a function of α and $\sqrt[3]{\psi_{30}}$. (b) (Top) The three stable configurations and (bottom) stochastic jumps in the cluster state recorded close to the transition point $\alpha \approx 1.24$, where the forward and backward barrier heights are equal. The octupole moment ψ_{30} is computed using the Abel transform.

ability to address individual ions, the diverse octupolar orders and rich energy landscapes that we present open up avenues for further research. By cooling the system to the motional ground state [53], the study of structural transitions can be extended to the quantum regime [54–57]. Introducing spin-spin interactions [18,20,58] between ions can enable the exploration of frustrated dynamics arising from competing charge and spin orders [21,59,60]—a frontier in quantum many-body physics.

More readily, the stochastic switching between different cluster configurations can be applied to study the kinetics of rare events. The ability to tune the barrier heights and noise sources (e.g., photon recoil) in 2D/3D energy landscapes [61,62] provides an ideal test bed for studies of thermal activation processes. The NEB method, which can accurately compute energy landscapes, can also be applied to engineer scalable trap architectures and protocols to realize ion reordering operations [63]. One can also employ these controllable 2D and 3D clusters to investigate stochastic resonance [64], pattern formation [65], heat transport and thermalization [66–68], dynamics in the presence of impurities [69] and topological defects [70–73], and Floquet engineering [74], broadening our understanding of collective nonlinear phenomena in the presence of long-range interactions.

Acknowledgments. We thank Arun Roy for comments on the manuscript. The authors acknowledge support from the Department of Science and Technology and the Ministry of Electronics and Information Technology, Government of India, under the "Centre for Excellence in Quantum Technologies" Grant with Ref. No. 4(7)/2020-ITEA. A. Paramekanti acknowledges funding via Discovery Grant No. RGPIN-2021-03214 from the Natural Sciences and Engineering Research Council (NSERC) of Canada.

Data availability. The data that support the findings of this article are not publicly available upon publication because it is not technically feasible and/or the cost of preparing, depositing, and hosting the data would be prohibitive within the terms of this research project. The data are available from the authors upon reasonable request.

Appendix A: Normal-mode excitation. We excite the motion of trapped ions in the experiment via two different methods. The first method is forced oscillation of the trap center, where one of the conical dc electrodes is given a small sinusoidal voltage, which results in the center of mass (c.o.m.) of the cluster oscillating about the trap center. When this frequency matches the c.o.m. mode's frequency, the increase in the oscillation amplitude of the ions is seen on electron multiplying charge-coupled device. Any slight misalignment of the conical electrode that is inadvertent leads to an oscillatory gradient field along both the radial and axial directions, enabling the excitation of both c.o.m. modes on resonance with this scheme. We directly measure α at different $U_{\rm dc}$ values by exciting a single ion's radial and axial motion. The second method is the amplitude modulation of rf voltage ($V_{\rm rf}$) at a frequency Ω_m. This leads to an oscillatory Mathieu q parameter, effectively modulating the elastic constants of the time-averaged harmonic potential, ω_x^2 and ω_z^2. This provides an alternative scheme for parametric excitation of the c.o.m. motion for $\Omega_m = 2 \times \omega_{x,z}$ [75].

TABLE I. Projections of the driven motion due to voltage modulation onto the 12 normal-mode eigenvectors of the four-ion cluster, with the soft mode contributions shown in bold font.

	Square ($\alpha = 1.254$)		Tetrahedron ($\alpha = 1.186$)	
Normal mode	ω_k/ω_x	$\lvert \boldsymbol{v}_m \cdot \boldsymbol{u}_k \rvert$	ω_k/ω_x	$\lvert \boldsymbol{v}_m \cdot \boldsymbol{u}_k \rvert$
Vibrational mode 1	1.73	1	1.76	0.09
Vibrational mode 2	1.49	0	1.37	0
Vibrational mode 3	1.32	0	1.35	0
Vibrational mode 4	1.32	0	1.35	0
c.o.m.—Z	1.254	0	1.186	0
c.o.m.—X	1	0	1	0
c.o.m.—Y	1	0	1	0
Vibrational mode 5	0.88	0	0.94	0
X rotation	0.76	0	0.52	0
Y rotation	0.76	0	0.52	0
Soft mode	**0.3**	**0**	**0.37**	**0.996**
Z rotation	0	0	0	0

However, in the case of a multi-ion cluster, the modulation of trap curvatures will also drive the ions about the equilibrium configuration $\boldsymbol{v}_0$ along the unit vector $\boldsymbol{v}_m$. We obtain this unit vector at a set of ($V_{\rm rf}$, $U_{\rm dc}$) values, by numerically computing the CME coordinates $\boldsymbol{v}_0^{\pm\delta}$ corresponding to small perturbation in rf voltage $V_{\rm rf}(1 \pm \delta)$. For small values of δ ($\sim 10^{-3}$),

$$\boldsymbol{v}_m = \frac{\boldsymbol{v}_0^{+\delta} - \boldsymbol{v}_0^{-\delta}}{\left|\left|\boldsymbol{v}_0^{+\delta} - \boldsymbol{v}_0^{-\delta}\right|\right|}. \tag{A1}$$

Collective normal modes (eigenvectors $\boldsymbol{u}_k$) that can couple to this drive have a finite projection $|\boldsymbol{v}_m \cdot \boldsymbol{u}_k|$.

Let us look at the effect of rf voltage modulation on the collective modes of four-ion cluster near the square to tetrahedron transition. The projections between the drive and the normal modes are tabulated in Table I. The symmetry-restoring soft mode of the tetrahedron (shown in Fig. 5) has a projection $\sim$1. The same technique, however, excites a high-frequency in-plane mode of the square shown in Fig. 5 and cannot be used to observe the softening of the square's symmetry-breaking mode.

Therefore, on the tetrahedron side, we experimentally excite the symmetry-restoring mode by rf voltage modulation, as shown by the responses captured in Figs. 2(b) and 6. The error bars in Fig. 2(c) are obtained from a Gaussian fit to the response captured across resonance. To visually demonstrate the resonant normal mode excitation via curvature modulation, we present a simple toy problem of two ions in a one-dimensional harmonic potential in Discussion III of the Supplemetal Material [46].

Appendix B: Buckling point of the five-ion pentagon. In the pentagonal configuration, the ion positions are given by $\mathbf{r}_n = (\rho \cos(\frac{2\pi n}{5}), \rho \sin(\frac{2\pi n}{5}), 0)$, where ρ is the circumradius of the pentagon. The total potential energy of the pentagonal

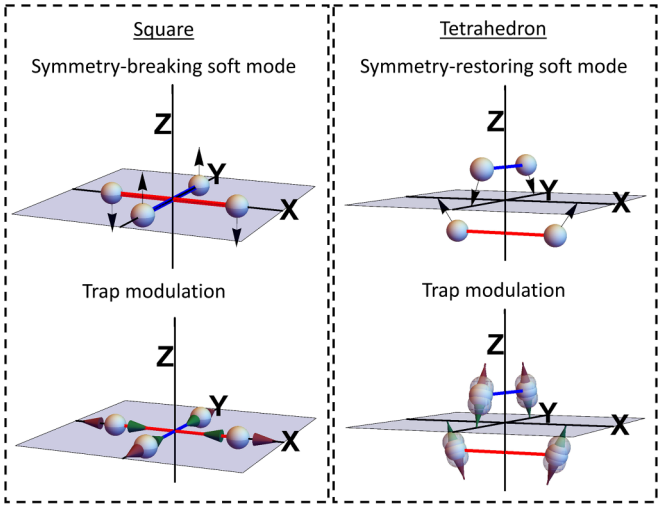


FIG. 5. (Top) Soft-mode eigenvectors of square and tetrahedron. (Bottom) The arrows with the same color represent in-phase motion of each ion due to trap voltage modulation.

configuration in scaled units is [46] $V(\rho) = 5\rho^2/2 + S_5/\rho$, where $S_5 = \sqrt{25 + 10\sqrt{5}}$. Minimizing with respect to ρ, we obtain the equilibrium radius $\rho_0^3 = S_5/5$.

The z displacements of the ions for the fundamental out-of-plane modes [35] can be described by sinusoidal functions of the ion index n (where $n = 0, 1, 2, 3, 4$):

$$z_n \propto \begin{cases} \cos\left(\frac{2\pi ln}{5}\right), & l = 0, 1, 2, \\ \sin\left(\frac{2\pi ln}{5}\right), & l = 1, 2, \end{cases} \tag{B1}$$

where l is an integer characterizing the angular dependence. The cosine l=0 mode corresponds to the c.o.m. oscillation of the entire cluster along the z axis. The l=1 modes correspond to rigid tilt/rotation about the x and y axes. The l=2 cosine and sine modes shown in Fig. 7 are the out-of-plane buckling modes.

The ion positions are slightly perturbed along the sine buckling mode $\mathbf{r}_n^0(\varepsilon) = (\rho_0 \cos(\frac{2\pi n}{5}), \rho_0 \sin(\frac{2\pi n}{5}), \varepsilon \sin(\frac{4\pi n}{5}))$. The change in harmonic potential energy is

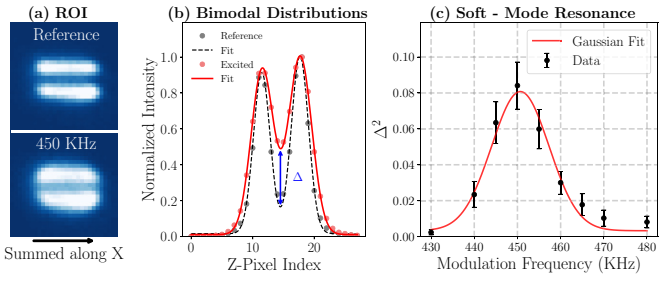


FIG. 6. Fitting procedure to obtain the soft-mode excitation frequency and its spread. (a) A reference frame is taken without the modulation, which is compared to the frames obtained at different modulation frequencies. (b) The deviation Δ is quantified from the change in bimodal distribution fit. (c) The deviation plotted against modulation frequency shows a resonance feature. A Gaussian is fit to obtain the center and its spread σ.

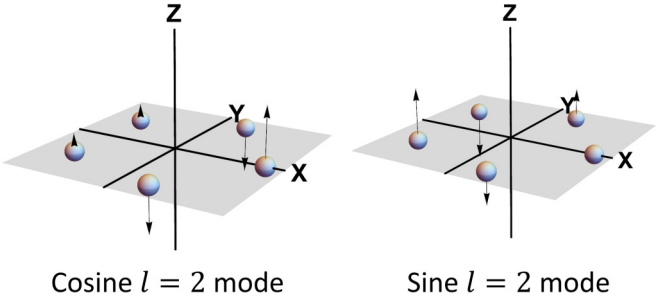


FIG. 7. Out-of-plane buckling modes of the five-ion pentagon.

positive, given by

$$\Delta V_{\text{trap}}^{(s)} = \frac{1}{2}\alpha^2\varepsilon^2 \sum_{n=0}^{4} \sin^2\left(\frac{4\pi n}{5}\right) = \frac{5}{4}\alpha^2\varepsilon^2. \tag{B2}$$

The distance between ions i and j changes to $|\mathbf{r}_i - \mathbf{r}_j| = \sqrt{(d_{ij}^0)^2 + (z_i^{(c)} - z_j^{(c)})^2}$, where the in-plane distance at the equilibrium configuration is $d_{ij}^0 = 2\rho^0 |\sin(\frac{\pi(i-j)}{5})|$. For small ε,

$$\frac{1}{|\mathbf{r}_i - \mathbf{r}_j|} = \frac{1}{d_{ij}^0}\left(1 + \frac{\left(z_i^{(c)} - z_j^{(c)}\right)^2}{\left(d_{ij}^0\right)^2}\right)^{-1/2}, \tag{B3}$$

$$\approx \frac{1}{d_{ij}^0}\left(1 - \frac{\left(z_i^{(c)} - z_j^{(c)}\right)^2}{2\left(d_{ij}^0\right)^2}\right), \tag{B4}$$

we arrive at the change in Coulomb energy

$$\Delta V_{\text{Coulomb}}^{(s)} = \sum_{i<j}\left(\frac{1}{|\mathbf{r}_i - \mathbf{r}_j|} - \frac{1}{d_{ij}^0}\right), \tag{B5}$$

$$\approx -\frac{\varepsilon^2}{16\rho_0^3}\sum_{i<j}\frac{\left[\sin\left(\frac{4\pi i}{5}\right) - \sin\left(\frac{4\pi j}{5}\right)\right]^2}{|\sin(\pi(i-j)/5)|^3}. \tag{B6}$$

Let us define the dimensionless structural sum as S_s. A similar analysis for the cosine mode leads to a structural sum $S_c = S_s$.

The change in total potential energy is

$$\Delta V_{\text{total}} = \left(\frac{5}{4}\alpha^2 - \frac{S_s}{16\rho_0^3}\right)\varepsilon^2 + \mathcal{O}(\varepsilon^4). \tag{B7}$$

The critical point of buckling (α_c) occurs when the coefficient of ε^2 changes sign at

$$\boxed{\alpha_c = \sqrt{\frac{S_s}{4S_5}} \approx 1.328.} \tag{B8}$$

Appendix C: Computing moments from images. The presence of cylindrical symmetry about z axis in our system permits us to apply Abel transforms [76,77] on the fluorescence images to reconstruct a time-averaged 3D charge distribution. Figure 8 shows the inverse Abel transform obtained for the six-ion 3D octahedral image; we use this method to compute octupole moments ψ_{30} for the five-ion hysteretic dynamics and the six-ion stochastic switching.

Appendix D: Numerical computations of the energy landscape. The equilibrium positions of the ions can be efficiently

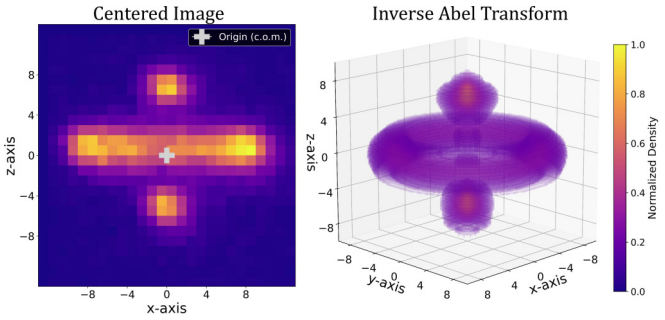


FIG. 8. Heat map showing the inverse Abel transform of the six-ion octahedron obtained from the corresponding fluorescence image.

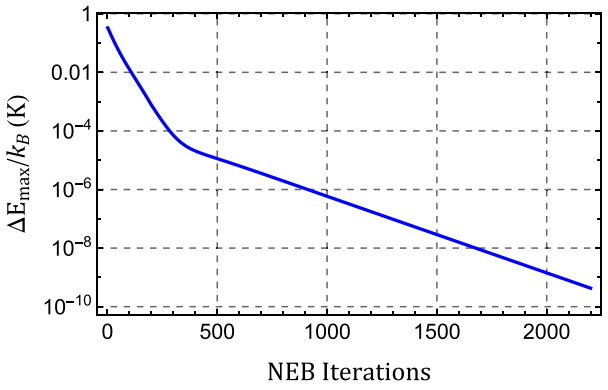


FIG. 9. Robustness of the saddle point determination. The plot shows the convergence of the difference in energy barrier heights (ΔE_{max}) obtained using the NEB method starting from two distinct initial guess paths. The rapid decay confirms that the saddle point identification is independent of the initial guess pathway.

obtained by minimizing the total potential energy [Eq. (1)] about a guess configuration, using the built-in *FindMinimum* function of Mathematica. For each α value, the initial guess configuration is randomized and then steered to a local minimum. This is repeated several times (up to 100) to identify the global minimum (CME). The collective-mode eigenvectors ($\boldsymbol{u}_k$) and corresponding frequencies (ω_k) are obtained from the Hessian matrix

$$H_{ij} = \left.\frac{\partial^2 V}{\partial v_i \partial v_j}\right|_{\boldsymbol{v}_0}, \tag{D1}$$

where v_i are the components of the vector $\boldsymbol{v} = (x_1, y_1, z_1, \ldots, x_n, y_n, z_n)$ and $\boldsymbol{v}_0$ is the coordinate of the equilibrium configuration (local or global minimum).

To obtain the minimum energy path (MEP) and the saddle point between two equilibrium configurations, we employ a chain-of-states method. A guess path between the stable equilibria is constructed using linear interpolation. The entire chain is taken to the MEP using the climbing-image variant of the NEB method [51]. To ensure the robustness of our energy landscapes, we verified that the calculations converge to the same saddle point regardless of the initial guess path. We constructed a distinct initial path using linear interpolation with a small perturbation (e.g., superimposing a sinusoid). As shown in Fig. 9, the difference in barrier heights ($\Delta E_{max} = E_{max}^{path\ 1} - E_{max}^{path\ 2}$) obtained from two such distinct initial paths converges toward zero. We further verified that the final spatial configurations of these two saddle points are almost identical.

In principle, NEB can lead to incorrect pathways when multiple minima are present in the energy landscape. To avoid convergence to incorrect saddle structures, we apply NEB between consecutive minima, sorted by a suitable order parameter. The final contour plots of energy landscapes shown in Figs. 3 and 4 are obtained by stitching MEPs between consecutive equilibrium configurations.

[1] S. A. Kivelson, J. M. Jiang, and J. Chang, *Statistical Mechanics of Phases and Phase Transitions*, 1st ed. (Princeton University Press, Princeton, NJ, 2024).

[2] P.-F. Lenne and V. Trivedi, Sculpting tissues by phase transitions, Nat. Commun. **13**, 664 (2022).

[3] D. Boyanovsky, H. J. de Vega, and D. J. Schwarz, Phase transitions in the early and present universe, Annu. Rev. Nucl. Part. Sci. **56**, 441 (2006).

[4] D. ter Haar, On the theory of phase transitions, *Collected Papers of L.D. Landau* (Pergamon Press, Oxford, UK, 1965), pp. 193–216.

[5] R. J. D. Miller, Femtosecond crystallography with ultrabright electrons and x-rays: Capturing chemistry in action, Science **343**, 1108 (2014).

[6] A. Cavalleri, *et al.*, Tracking the motion of charges in a terahertz light field by femtosecond x-ray diffraction, Nature (London) **442**, 664 (2006).

[7] E. J. Sie, *et al.*, An ultrafast symmetry switch in a Weyl semimetal, Nature (London) **565**, 61 (2019).

[8] A. de la Torre, *et al.*, *Colloquium:* Nonthermal pathways to ultrafast control in quantum materials, Rev. Mod. Phys. **93**, 041002 (2021).

[9] J. Ho, *et al.*, Optomechanical self-organization in a mesoscopic atom array, Nat. Phys. **21**, 1071 (2025).

[10] W. Cochran, *The Dynamics of Atoms in Crystals* (Edward Arnold Limited, Great Britain, 1973).

[11] C. V. Raman and T. M. K. Nedungadi, The α–β transformation of quartz, Nature (London) **145**, 147 (1940).

[12] W. Cochran, Crystal stability and the theory of ferroelectricity, Phys. Rev. Lett. **3**, 412 (1959).

[13] P. W. Anderson, Qualitative considerations on the statistics of the phase transition in $BaTiO_3$-type ferroelectrics, Career Theor. Phys. **35**, 61 (2005).

[14] P. Tolédano and V. Dmitriev, *Reconstructive Phase Transitions: In Crystals and Quasicrystals* (World Scientific, Singapore, 1996).

[15] X.-J. Yan, *et al.*, Investigation on the phase-transition-induced hysteresis in the thermal transport along the *c*-axis of $MoTe_2$, npj Quantum Mater. **2**, 31 (2017).

[16] M. S. Akhanda, *et al.*, Phase-transition-induced thermal hysteresis in type-II Weyl semimetals $MoTe_2$ and $Mo_{1-x}W_xTe_2$, Mater. Today Phys. **29**, 100918 (2022).

[17] J. C. Tolédano and P. Tolédano, *The Landau Theory of Phase Transitions: Application to Structural, Incommensurate, Mag-*

netic and Liquid Crystal Systems (World Scientific, Singapore, 1987).
[18] R. Blatt and C. F. Roos, Quantum simulations with trapped ions, Nat. Phys. **8**, 277 (2012).
[19] M. Drewsen, Ion Coulomb crystals, Phys. B **460**, 105 (2015).
[20] C. Monroe, *et al.*, Programmable quantum simulations of spin systems with trapped ions, Rev. Mod. Phys. **93**, 025001 (2021).
[21] Z. Sun, Y. H. Teoh, F. Rajabi, and R. Islam, Two-dimensional ion crystals in a hybrid optical cavity trap for quantum information processing, Phys. Rev. A **109**, 032426 (2024).
[22] G. Morigi, *et al.*, Ion Coulomb crystals: an exotic form of condensed matter, arXiv:2508.07374.
[23] D. J. Wineland, J. C. Bergquist, W. M. Itano, J. J. Bollinger, and C.H. Manney, Atomic-ion Coulomb clusters in an ion trap, Phys. Rev. Lett. **59**, 2935 (1987).
[24] D. H. E. Dubin, Theory of structural phase transitions in a trapped Coulomb crystal, Phys. Rev. Lett. **71**, 2753 (1993).
[25] J. P. Schiffer, Phase transitions in anisotropically confined ionic crystals, Phys. Rev. Lett. **70**, 818 (1993).
[26] T. B. Mitchell, *et al.*, Direct observations of structural phase transitions in planar crystallized ion plasmas, Science **282**, 1290 (1998).
[27] S. L. Gilbert, J. J. Bollinger, and D. J. Wineland, Shell-structure phase of magnetically confined strongly coupled plasmas, Phys. Rev. Lett. **60**, 2022 (1988).
[28] J. N. Tan, J. J. Bollinger, B. Jelenkovic, and D. J. Wineland, Long-range order in laser-cooled, atomic-ion Wigner crystals observed by Bragg scattering, Phys. Rev. Lett. **75**, 4198 (1995).
[29] M. Drewsen, C. Brodersen, L. Hornekaer, J. S. Hangst, and J. P. Schiffer, Large ion crystals in a linear Paul trap, Phys. Rev. Lett. **81**, 2878 (1998).
[30] A. Mortensen, E. Nielsen, T. Matthey, and M. Drewsen, Observation of three-dimensional long-range order in small ion Coulomb crystals in an rf trap, Phys. Rev. Lett. **96**, 103001 (2006).
[31] Y. Ibaraki, U. Tanaka, and S. Urabe, Detection of parametric resonance of trapped ions for micromotion compensation, Appl. Phys. B **105**, 219 (2011).
[32] J. Kiethe, L. Timm, H. Landa, D. Kalincev, G. Morigi, and T. E. Mehlstaubler, Finite-temperature spectrum at the symmetry-breaking linear to zigzag transition, Phys. Rev. B **103**, 104106 (2021).
[33] J. Kiethe, *et al.*, Probing nanofriction and Aubry-type signatures in a finite self-organized system, Nat. Commun. **8**, 15364 (2017).
[34] J. Zhang, *et al.*, Spectroscopic characterization of the quantum linear-zigzag transition in trapped ions, npj Quantum Inf. **9**, 68 (2023).
[35] D. Podolsky, E. Shimshoni, G. Morigi, and S. Fishman, Buckling transitions and clock order of two-dimensional Coulomb crystals, Phys. Rev. X **6**, 031025 (2016).
[36] J. W. Harter and others, A parity-breaking electronic nematic phase transition in the spin-orbit coupled metal $Cd_2Re_2O_7$, Science **356**, 295 (2017).
[37] H. Ning, *et al.*, A coherent phonon-induced hidden quadrupolar ordered state in Ca_2RuO_4, Nat. Commun. **14**, 8258 (2023).
[38] S. Voleti, *et al.*, Probing octupolar hidden order via Janus impurities, npj Quantum Mater. **8**, 42 (2023).
[39] L. Ye, *et al.*, Measurement of the magnetic octupole susceptibility of PrV_2Al_20, Nat. Commun. **15**, 7005 (2024).
[40] R. F. Casten, Shape phase transitions and critical-point phenomena in atomic nuclei, Nat. Phys. **2**, 811 (2006).
[41] S. Rajbanshi, *et al.*, Experimental evidence of exact E(5) symmetry in ^{82}Kr, Phys. Rev. C **104**, L031302 (2021).
[42] S. Zhao, H. J. Xu, Y. Zhou, Y. X. Liu, and H. Song, Exploring the nuclear-shape phase transition in ultrarelativistic $^{129}Xe + ^{129}Xe$ collisions at the lhc, Phys. Rev. Lett. **133**, 192301 (2024).
[43] A. Prakash, A. Ayyadevara, E. Krishnakumar, and S. A. Rangwala, Low divergence cold-wall oven for loading ion traps, Rev. Sci. Instrum. **95**, 033202 (2024).
[44] C. A. Schrama, E. Peik, W. W. Smith, and H. Walther, Novel miniature ion traps, Opt. Commun. **101**, 32 (1993).
[45] A. Prakash, *et al.*, Endcap-type Paul trap for precision spectroscopy and studies of controlled interactions, arXiv:2601.07328.
[46] See Supplemental Material at http://link.aps.org/supplemental/10.1103/2rs1-c5r1 for a description of the experimental setup, analytical calculations of the transition points, and numerically computed normal-mode spectra of equilibrium configurations, which also includes Refs. [45,78–81].
[47] D. H. E. Dubin and T. M. O'Neil, Trapped nonneutral plasmas, liquids, and crystals (the thermal equilibrium states), Rev. Mod. Phys. **71**, 87 (1999).
[48] S. H. Strogatz, *Nonlinear Dynamics and Chaos: With Applications to Physics, Biology, Chemistry, and Engineering*, 2nd ed. (CRC Press, Boca Raton, 2015).
[49] D. Podolsky, A. Auerbach, and D. P. Arovas, Visibility of the amplitude (Higgs) mode in condensed matter, Phys. Rev. B **84**, 174522 (2011).
[50] M. Endres, *et al.*, The 'Higgs' amplitude mode at the two-dimensional superfluid/Mott insulator transition, Nature (London) **487**, 454 (2012).
[51] G. Henkelman, B. P. Uberuaga, and H. Jónsson, A climbing image nudged elastic band method for finding saddle points and minimum energy paths, J. Chem. Phys. **113**, 9901 (2000).
[52] S. A. Jackson, P. A. Lee, and T. M. Rice, Triple point of the lock-in and onset transitions of charge-density waves, Phys. Rev. B **17**, 3611 (1978).
[53] E. Jordan, K. A. Gilmore, A. Shankar, A. Safavi-Naini, J. G. Bohnet, M. J. Holland, and J. J. Bollinger, Near ground-state cooling of two-dimensional trapped-ion crystals with more than 100 ions, Phys. Rev. Lett. **122**, 053603 (2019).
[54] A. Retzker, R. C. Thompson, D. M. Segal, and M. B. Plenio, Double well potentials and quantum phase transitions in ion traps, Phys. Rev. Lett. **101**, 260504 (2008).
[55] E. Shimshoni, G. Morigi, and S. Fishman, Quantum zigzag transition in ion chains, Phys. Rev. Lett. **106**, 010401 (2011).
[56] R. Puebla, Structural Phase Transitions, in *Equilibrium and Nonequilibrium Aspects of Phase Transitions in Quantum Physics, Springer Theses* (Springer, Cham, 2018), pp. 25–53.
[57] P. M. Bonetti, A. Rucci, M. L. Chiofalo, and V. Vuletić, Quantum effects in the Aubry transition, Phys. Rev. Res. **3**, 013031 (2021).
[58] J. Britton, *et al.*, Engineered two-dimensional Ising interactions in a trapped-ion quantum simulator with hundreds of spins, Nature (London) **484**, 489 (2012).
[59] R. Nath, *et al.*, Hexagonal plaquette spin–spin interactions and quantum magnetism in a two-dimensional ion crystal, New J. Phys. **17**, 065018 (2015).

[60] M. Qiao, *et al.*, Observing frustrated quantum magnetism in two-dimensional ion crystals, arXiv:2204.07283.

[61] N. Mizukami, G. Gatta, L. Duca, and C. Sias, Emulating isomerization with two-dimensional Coulomb crystals, arXiv:2508.05902.

[62] A. Ayyadevara, A. Prakash, S. Dutta, A. Paramekanti, and S. A. Rangwala, Symmetry-controlled thermal activation in pyramidal Coulomb clusters: Testing Kramers-Langer theory, arXiv:2601.04883.

[63] R. D. Delaney, *et al.*, Scalable multispecies ion transport in a grid-based surface-electrode trap, Phys. Rev. X **14**, 041028 (2024).

[64] Q. Yuan, *et al.*, Stochastic resonance via single-ion phonon laser, Appl. Phys. Lett. **125**, 102201 (2024).

[65] T. E. Lee and M. C. Cross, Pattern formation with trapped ions, Phys. Rev. Lett. **106**, 143001 (2011).

[66] A. Bermudez, M. Bruderer, and M. B. Plenio, Controlling and measuring quantum transport of heat in trapped-ion crystals, Phys. Rev. Lett. **111**, 040601 (2013).

[67] N. Freitas, E. A. Martinez, and J. P. Paz, Heat transport through ion crystals, Phys. Scr. **91**, 013007 (2016).

[68] L. Timm, H. Weimer, L. Santos, and T. E. Mehlstäubler, Heat transport in an ion Coulomb crystal with a topological defect, Phys. Rev. B **108**, 134302 (2023).

[69] L. Duca, N. Mizukami, E. Perego, M. Inguscio, and C. Sias, Orientational melting in a mesoscopic system of charged particles, Phys. Rev. Lett. **131**, 083602 (2023).

[70] A. delCampo, G. Dechiara, G. Morigi, M. B. Plenio, and A. Retzker, Structural defects in ion chains by quenching the external potential: The inhomogeneous Kibble-Zurek mechanism, Phys. Rev. Lett. **105**, 075701 (2010).

[71] S. Ulm, *et al.*, Observation of the Kibble–Zurek scaling law for defect formation in ion crystals, Nat. Commun. **4**, 2290 (2013).

[72] K. Pyka, *et al.*, Topological defect formation and spontaneous symmetry breaking in ion Coulomb crystals, Nat. Commun. **4**, 2291 (2013).

[73] M. Arnold and R. Nigmatullin, Dynamics of vortex defect formation in two-dimensional Coulomb crystals, Phys. Rev. B **106**, 104106 (2022).

[74] P. Kiefer, F. Hakelberg, M. Wittemer, A. Bermudez, D. Porras, U. Warring, and T. Schaetz, Floquet-engineered vibrational dynamics in a two-dimensional array of trapped ions, Phys. Rev. Lett. **123**, 213605 (2019).

[75] J. Schmidt, *et al.*, Mass-selective removal of ions from Paul traps using parametric excitation, Appl. Phys. B **126**, 176 (2020).

[76] N. H. Abel, Résolution d'un problème de mécanique, J. Reine Angew. Math. **1**, 153 (1826).

[77] D. D. Hickstein, *et al.*, A direct comparison of high-speed methods for the numerical Abel transform, Rev. Sci. Instrum. **90**, 065115 (2019).

[78] P. B. R. Nisbet-Jones, *et al.*, A single-ion trap with minimized ion–environment interactions, Appl. Phys. B **122**, 57 (2016).

[79] T. Lindvall, K. J. Hanhijärvi, T. Fordell, and A. E. Wallin, High-accuracy determination of Paul-trap stability parameters for electric-quadrupole-shift prediction, J. Appl. Phys. **132**, 124401 (2022).

[80] F. G. Major, V. N. Gheorghe, and G. Werth, *Charged Particle Traps* (Springer, Berlin, 2005).

[81] D. Leibfried, R. Blatt, C. Monroe, and D. Wineland, Quantum dynamics of single trapped ions, Rev. Mod. Phys. **75**, 281 (2003).